

Hybrid Topological Defects in Ferroelectric Nematic Fluids

Shengzhu Yi^{1,2}, Chao Zhou¹, Zening Hong¹, Zhongjie Ma¹, Mingjun Huang^{3,4}, Satoshi Aya^{3,4}, Rui Zhang², Qi-Huo Wei^{1,5*}

¹State Key Laboratory of Quantum Functional Materials, Department of Mechanical and Energy Engineering, Southern University of Science and Technology, Shenzhen, 518055, China

²Department of physics, The Hongkong University of Science and Technology, Clear Water Bay, Hong Kong, China

³South China Advanced Institute for Soft Matter Science and Technology (AISMST), School of Emergent Soft Matter, South China University of Technology, Guangzhou 510640, China

⁴Guangdong Provincial Key Laboratory of Functional and Intelligent Hybrid Materials and Devices, South China University of Technology, Guangzhou 510640, China

⁵Center for Complex Flows and Soft Matter Research, Southern University of Science and Technology, Shenzhen 518055, China

Email: weiqh@sustech.edu.cn

Field theories predict that phase transitions sequentially breaking continuous and discrete symmetries can generate hybrid topological structures in which defects of different dimensionalities merge. We report experimental and numerical studies of hybrid defects in ferroelectric nematic liquid crystals, which undergo a cascaded transition from isotropic liquid to a high-symmetry apolar, and then to a low-symmetry polar nematic phase. By imposing surface anchoring to preset disclination configurations, we directly track the transformation of topological defects across the transition. We show that simple disclinations reproducibly evolve into complex hybrid states, including domain walls terminated by surface disclinations, domain walls decorated with monopoles, and merons-mediated boojums and monopoles. These results provide definitive experimental validation of hybrid defects in a soft matter system and establish ferroelectric nematics as a model platform for exploring and engineering polar defect structures.

Introduction

Topological defects, singular configurations in ordered media, are ubiquitous hallmarks of broken symmetry (1). These defects emerge across a vast range of scales, from the nascent universe (2, 3) to diverse condensed matter systems like superfluid ^3He (1, 4), ferroic materials (5, 6), and liquid crystals (7–9). The emergence and proliferation dynamics of topological defects during spontaneous symmetry breaking transitions have been described in field theories by Kibble and Zurek for cosmic defects like strings and domain walls (10, 11). This theoretical framework was subsequently extended to predict that sequential phase transitions, involving the breaking of both continuous and discrete symmetries, could yield hybrid structures where defects of different dimensionalities intertwine (3, 12). Typically, the breaking of a continuous symmetry generates line defects (strings), whereas the breaking of a discrete symmetry produces domain walls bounded by strings.

The universality of symmetry-breaking concepts, coupled with the difficulty of directly detecting cosmological structures, has driven the search for analogs in condensed matter systems such as superfluid ^3He (13) and liquid crystals (14, 15). Traditional liquid crystals, composed of rod-like molecules, can align along a common direction called the director (\mathbf{n}), forming the nematic phase. Upon cooling, they transition from an isotropic phase (I) with full symmetry to the nematic phase that retains rotational symmetry [SO(2)] only around the director \mathbf{n} and the head-to-tail symmetry (\mathbb{Z}_2) of \mathbf{n} , thereby breaking continuous rotational symmetry (1, 8). These conventional liquid crystals have been an exceptional laboratory system for both validating the Kibble-Zurek mechanism (14, 15) and exploring intriguing properties of topological defects (16–18).

A newly discovered class of polar liquid crystals exhibits an additional transition from the apolar nematic phase to a polar nematic (N_F) phase characterized by a spontaneous polarization, \mathbf{P} (19–22). This secondary transition breaks discrete inversion symmetry (\mathbb{Z}_2) and reduces the symmetry to $SO(2)$, providing a physical realization of the symmetry-breaking cascade envisioned by Kibble. Formations of hybrid topological defects in the N_F phase have been proposed while direct evidence remains absent (22, 23). The N – N_F transition is known to host a wealth of topological defects and associated dynamical phenomena (24–30); yet the evolutionary pathways of these polar defects and their connection to polar symmetry remain to be fully understood.

Here, we investigate how string defects or disclinations, transform when polar fluids are quenched from the nematic to the ferroelectric nematic phase. By imposing predesigned director fields at confining surfaces, we generate well-defined topological defects and track their evolution using polarized optical microscopy and numerical simulations based on Landau–de Gennes and Ericksen–Leslie theories. We show that nematic disclinations invariably reorganize into hybrid topological states—where domain walls, surface disclinations, monopoles and merons are intertwined—driven by a fundamental reshaping of the ground-state manifold under discrete symmetry breaking. These findings provide experimental verification of cosmological theory on cascade symmetry breaking and establish a conceptual framework for understanding and engineering polar topology in ferroelectric nematic liquids.

Results

Ground State Manifold and Homotopy in Apolar and Polar Nematic

The polar liquid studied here is the 4-[(4-nitrophenoxy)carbonyl]phenyl 2,4-dimethoxybenzoate (RM734). Its phase sequence is I–187°C–N–133°C– N_F –84°C–Crystal (Fig. 1a&b). Each phase transition entails a distinct symmetry breaking that reshapes the set of degenerate states or the ground-state manifold. In the N phase, the ground state manifold can be viewed as a sphere with diametrically opposite points identified, namely the real projective plane (\mathbb{RP}^2) where each pair of antipodal points on its surface represents a possible orientation of the director \mathbf{n} . In the N_F phase, the ground-state manifold becomes a spherical surface (\mathbb{S}^2).

This change in the ground-state manifold alters the distinct sets of mappings that characterize topological defects, i.e. the homotopy groups (1, 8, 9). In the N phase, half-integer line defects are topologically stable. When one traces a closed loop encircling such a defect, the director field projects onto the \mathbb{RP}^2 manifold as continuous path connecting antipodal points (Fig. 1c). In contrast, within the N_F phase, half-integer disclinations cannot exist as isolated structures as their mapping sweeps only half of a great circle on the \mathbb{S}^2 manifold. Consequently, these defects need to be bounded to domain walls where the orientation undergoes a π flip (Fig. 1d).

Integer disclinations, by comparison, lack topological stability in both the N and N_F phases. A loop around an integer-defect maps to a loop on the manifold, which can continuously shrink to a point, allowing the singularity to be smoothly eliminated (Fig. 1e). In the N phase, rather than disappearing, an integer disclination typically dissociates into a pair of stable half-integer disclinations. This process is energetically favored because the elastic free energy scales with the square of the topological charge, splitting a +1 defect into two +1/2 defects lowers the total energy by half (31).

To investigate how the shift of ground-state manifold influences topological defects, we fabricated liquid crystal cells using high-resolution photopatterning (32, 33). This technique allowed us to define the director field, $\mathbf{n}(x, y) = [\cos \theta(x, y), \sin \theta(x, y), 0]$, at the confining surfaces. The director orientation $\theta(x, y)$ was identical on both substrates and described by:

$$\theta(x, y) = \sum_i q_i \tan^{-1}[(y - y_{0i})/(x - x_{0i})] + \alpha \quad (1)$$

where q_i is the topological charge of the i -th defect located at (x_{0i}, y_{0i}) , and α is a constant phase offset. To prevent polarization twisting, which can occur in thicker samples (34, 35), we used thin cells with a thickness of less than 3 μm .

$\pm 1/2$ Disclination Pair Transforming into a π Wall Terminated by Surface Disclinations

We first explored a pair of $\pm 1/2$ disclinations, with a director field described by Eq. 1 with $q_{1,2} = \pm 1/2$ and $\alpha = \pi/2$. In this configuration, the director aligns parallel to the line connecting the two defects but gradually rotates to become perpendicular in the far field (Fig. 2a). This director pattern was proposed by Lavrentovich as an intriguing pathway to forming a π wall bounded by vertical half-integer disclinations, where the polarizations beside the wall point in opposite directions (22).

Upon entering the N phase via the I-N transition, the liquid crystal's director field precisely matches the imprinted pattern, resulting in two half-integer disclinations. These were confirmed by the appearance of two black brushes under crossed polarized optical microscopy and through director field measurements using the PolScope technique (36) (Fig. 2b&c).

Numerical simulations, based on the Landau–de Gennes theory (detailed in supplementary materials) (37), reveal two possible defect configurations, depending on cell thickness: (i) in thin cells two vertical lines bridging the point defects that bend towards each other (Fig. 2g), and (ii) in thick cells two horizontal line defects connecting the $+1/2$ and $-1/2$ defects (Fig. S1). Our experimental condition corresponds to the first case.

Upon entering the N_F phase via cooling, two black lines extended from the $+1/2$ and $-1/2$ disclinations and merged into a continuous wall (Movie S1). Concurrently, the black brushes between the defects vanished (Fig. 2d), a signature of director twist under crossed polarizers. This twist was confirmed by measuring optical transmittance (T) as a function of the angle γ between the polarizer and analyzer. In contrast to non-twist nematic cell where $T(\gamma) \propto \cos^2\gamma$ (31), the optical transmittance in the square regions does not go to extinct (Fig. 2f), demonstrating the director twist along the cell normal.

Numerical calculations using an extended Ericksen–Leslie model (see Methods) (38, 39) show that the defect configuration in the N_F phase corresponds to a domain wall composed of two surface line defects (Fig. 2h). Mapping the polarization along a semicircle around these surface defects traces a half-circle connecting antipodal points on the S^2 manifold, confirming their identity as half-integer surface disclinations (Fig. 2i). Near these defects, the polarization undergoes a sharp π reversal, while at the cell mid-plane it remains uniformly aligned. This difference produces a polarization twist along the cell normal. Using the simulated polarization field, we computed the transmittance as a function of γ using the Jones matrix method and obtained quantitative agreement with experiment (red dashed line in Fig. 2f).

The surface line defects in the N_F phase remain tightly bound to the confining substrates (Fig. 2k&l), in sharp contrast to the N phase, where line defects adopt arc-like shapes due to repulsion from planar anchoring (Fig. S1). In the N_F phase, half-integer line defects cannot exist independently in the bulk and thus must adhere to the liquid-crystal/substrate interface. This confinement arises from a topological constraint, which imposes an infinite energy barrier against detaching a half-integer surface line defect into the bulk.

The walls terminated by two surface disclinations are common in the polar fluids. As shown in a previous study, the π walls are composed of twin surface disclinations separated horizontally (39, 40). The horizontal separation distance between the two lines scales proportionally with the cell thickness. In this study, the two lines exhibit a much smaller separation distance. This is attributed to the thin cell thickness (1.5 μm) and the aligned director patterns at two substrates.

$+1/2$ Disclination Pair Transforming into a Monopole-Embedded π Wall

The second configuration considered is a pair of $+1/2$ defects with a director field described by Eq. 1 with $q_{1,2} = +1/2$ and $\alpha = \pi/2$. The two $+1/2$ defects are arranged head-to-head so that the

director near the line connecting two defects is parallel to the line. Far from the origin, this director field is equivalent to a +1 defect of concentric configuration (Fig. 3a).

In the N phase, optical textures under polarized optical microscopy display two dark brushes emanating from the defect centers (Fig. 3b). PolScope measurements confirm a two-dimensional director field that aligns well with the predesigned pattern. Numerical calculations reveal that these defects are two vertical disclinations linking the point defects at the two confining surfaces (Fig. 3f). Note that the formation of two horizontal disclinations, connecting defects on the same surfaces, is topologically prohibited, because it would result in a middle plane devoid of singularities, inconsistent with the non-trivial topological charges.

Upon entering the N_F phase, the characteristic four-brush texture is retained. The key difference is the appearance of a point defect at the center of a black wall, most evident under bright-field imaging (Movie S2; Fig. 3c). This contrasts with the smooth domain wall observed in the ±1/2 defect pair. Optical transmittance measurements show $T(\gamma) \propto \cos^2\gamma$ (Fig. 3e), indicating the absence of director twist across the cell. PolScope imaging further confirms that the director near the wall remains largely parallel to it (Fig. 3c). These results demonstrate that the orientation field is preserved through the phase transition, with the wall region as the sole exception.

Numerical calculations further reveal that the N_F topological structure is a π wall embedded with a point defect (Fig. 3g). The wall is terminated by two surface disclinations connecting a pair of +1/2 defects at the confining surfaces, with antiparallel polarizations on either side (Fig. 3h). These disclinations carry a net topological charge of $q = q_1 + q_2$, and can transform continuously into a +1 point defect as two +1/2 defects move closer to merge. This behavior contrasts sharply with the topologically trivial wall formed by the ±1/2 defect pair where the sum of the topological charges yields $q = 0$ (Fig. 2k).

To characterize the point defect between the confining surfaces, we map the polarization on a spherical surface surrounding its core onto the ground-state manifold. This mapping completely covers the S^2 surface, indicating that the defect is a monopole with winding number 1 (Fig. 3i). Furthermore, in any xy -plane located between the monopole and the surface defects, the far-field polarizations remain confined to the xy -plane, whereas at the center they point vertically (Fig. 3j-k). Mapping these polarizations in the xy -plane onto the S^2 ground state manifold reveals that polarizations located above and below the midplane correspond to the coverage of the upper and lower hemispheres, respectively. This mapping indicates that the topological structures within these planes are merons (also called half Skyrmions).

Monopoles are common along π walls in the N_F phase. A representative optical image shown in Fig. S2 highlights π domain walls that arise under uniform surface alignment conditions. As established in prior work, a π domain wall formed under these conditions consists of twin surface disclinations enclosing a chiral subdomain (39). Within this subdomain, the polarization undergoes a π twist across the cell. Both the disclination configuration and the subdomain chirality have two degenerate states. Simultaneous reversal of the subdomain's chirality and the twin disclination configuration generates kinks and anti-kinks (39). By contrast, point defects—identified in numerical studies as monopoles (Fig. S3, see supplementary materials)—emerge when only the subdomain chirality is inverted (Movie S3, Fig. 3d).

+1 Disclination Transforming into Meron-Mediated Monopole and Boojums

We next examine a +1 defect where the director field is described by Eq. 1, with $q_1 = +1$ and $\alpha = 0$. In this design, the radial director exhibits pure splay deformations (Fig. 4a). In the N phase, the optical texture reveals two defect cores, each associated with two black brushes, characteristic of half-integer strength. Our simulations further resolve the splitting into two +1/2 disclinations, highlighting both the director fields and the reduced order parameter at the cores of the two +1/2 defects in the cell's middle plane (Fig. 4c).

As the liquid crystal enters the N_F phase, the optical textures of two +1/2 defects coalesce into a single defect characterized by four dark brushes (Movie S4, Figs. S4 and 4b). These dark brushes

form a distinctive pinwheel structure, which adopt either left- or right-handed twist with equal probability. By analyzing the response of this spiral texture to an in-plane electric field, we determined that the polarization points outward (Fig. S4), indicating that \mathbf{P} is aligned parallel to $\mathbf{n}(\nabla \cdot \mathbf{n})$. This specific polarization direction can be attributed to flexoelectric effect during the N-N_F phase transition. The RM734 a positive flexoelectric coupling coefficient (λ) (35, 41). This parallel alignment minimizes the associated free energy, as described by: $F_{\text{Flexo}} = -\lambda \int d\mathbf{r}^3 \mathbf{n}(\nabla \cdot \mathbf{n}) \cdot \mathbf{P}$ (41, 42).

Numerically calculated polarization fields show that the spiral texture originates from a composite structure, consisting of a point defect in the mid-plane of the cell together with two additional point defects at the confining surfaces (Fig. 4d). The polarization field in the mid-plane (Fig. 4e) contains a defect core with vanishing polarization, around which the director field is dominated by bend instead of splay deformations. This transformation, shifting from a splay-dominated to a bend-dominated polarization field, stems from the minimization of electrostatic interactions. Splay in polarizations generates a bound charge density ($\rho = -\nabla \cdot \mathbf{P}$). When these charges remain unscreened by free ions, their strong Coulombic interactions would lead to a substantial increase in electrostatic energy, effectively raising the cost of splay deformations. The veracity of our calculated polarization field is confirmed by its ability to accurately reproduce the spiral optical textures seen in experimental observations (Fig. 4f).

To ascertain the topological character of these point defects, we mapped the polarization field onto the ground-state manifold. Projecting the polarization on a spherical surface enclosing the middle defect yields complete coverage of S^2 , identifying the defect as a monopole with winding number 1 (Fig. 4g). By contrast, mapping the polarization on hemispherical surfaces centered on individual surface-defect cores produces coverage restricted to a single hemisphere of the manifold (Fig. 4h), establishing these surface defects as half-monopoles, or boojums.

The polarization fields in the planes between point defects exhibit a characteristic pattern: at the core, the polarization is oriented perpendicular to the xy -plane, while at the periphery it lies entirely in-plane (Fig. 4i, j). This configuration corresponds to a $\pi/2$ rotation from the center to the boundary, a defining feature of merons. When the polarization in the xy -plane is mapped onto the ground-state manifold, it covers the entirety of either the upper or lower hemisphere, thereby confirming their identification as merons (Fig. 4i, j).

Discussion

These findings provide a tabletop validation of Kibble's prediction regarding hybrid defects, while also offering a broader framework for understanding polar topological structures in ferroelectric nematic fluids. The hybrid and three-dimensional configurations we identified can help clarify previously reported topological structures, such as paired domain walls (24), point defects within walls (43), and spiral textures (28, 44). Hybrid topological defects are commonly observed during apolar-to-polar nematic phase transitions (see Movie S5 and Fig. S5). Another compelling example is the -1 disclination, which splits into two half-integer disclinations in the apolar phase but transforms into a wall vertex in the polar phase (Movie S6 and Fig. S6). These vertex walls, aligned along director fields that point toward the defect core, form hybrid topological defects made up of π walls and monopoles.

Polar topological defects have garnered significant attention due to their fundamental importance and potential technological applications (6). In solid-state ferroelectrics, the polarization vector is constrained by lattice symmetry, as dictated by Neumann's theorem (45). As a result, creating polar defects requires precise control over confinement geometries and strain fields (46–48). In contrast, ferroelectric nematic liquid crystals maintain continuous translational symmetry, allowing topological defects to emerge naturally from the symmetry of the polar field. Here we demonstrate a practical strategy to engineer hybrid polar defects with tunable morphology and spatial organization by precisely patterning directors on confining substrates. Figure S7 illustrates an example of such hybrid defect arrays. The design space can be further expanded by combining

photopatterning with the flexoelectric effect (42) and exploring emerging polar fluidic materials that host novel ground states (49–51).

Ferroelectric nematic fluids exhibit exceptionally large second-order nonlinear optical coefficients (18, 48), offering new opportunities in nonlinear and quantum optics through their intrinsic tunability (53). With dimensions comparable to optical wavelengths, hybrid defects provide a versatile platform for controlling light topology in nonlinear interactions (26, 44, 54). Their hybrid and inherently three-dimensional character are key to unlocking such applications.

Materials and Methods

Photo-patterned Cells

Liquid crystal cells were prepared using glass substrates subjected to thorough cleaning: 30 min of ultrasonic treatment in an aqueous detergent solution, followed by 10 min of ultraviolet and oxygen plasma exposure. After cleaning, a thin layer of the photoalignment material SD1 (azobenzene dye, 0.5 wt% in dimethylformamide) was deposited by spin coating at 500 rpm for 10 s and 3000 rpm for 30 s. Cells were assembled by pairing two SD1-coated substrates, with silica beads (1–3 μm) serving as spacers to define the cell thickness. The predesigned director patterns were then imprinted into the SD1 layer using a photopatterning technique.

Two experimental factors are proved essential for generating well-organized hybrid topological defects. First, the spatial resolution of director photopatterning plays a critical role. Second, charge neutrality of the photopatterned defect arrays needs to be preserved by arranging positive and negative defects in periodic arrays, with a typical spacing of $\sim 20 \mu\text{m}$. We found that such tessellation of defect patterns suppresses the propagation of domain walls through the patterned defects.

In a prior study (27), Lavrentovich et al imprinted a single radial defect of 200 μm in diameter on confining substrates and observed pie-slice-like domains divided by π walls, where \mathbf{P} was either parallel or anti-parallel to the radial direction. This configuration differs from the fine pinwheel structure observed here (Fig. 4). The discrepancy likely stems from differences in the precision of the photopatterning technique, the defect size and the topological constraints imposed by the defect arrays.

Mechanically Rubbed Cells

The aligning agent was prepared by mixing polyimide (PI-2555, HD MicroSystems, Ltd.) with dimethylformamide at a 1:9 mass ratio. Glass substrates were ultrasonically cleaned in deionized water and dried under a nitrogen stream before spin coating. The PI-2555 solution was deposited by spin coating at 500 rpm for 10 s, followed by 4000 rpm for 30 s, and then baked at 200 °C for 90 mins. The resulting PI-2555 layer was unidirectionally buffed using a roller ($\sim 10 \text{ mm}$ diameter) wrapped with 2 mm flannel, rotated at $\sim 30 \text{ rad/s}$ for 5 s. Cells were assembled using two those treated substrates with their rubbing directions aligned in parallel.

Numerical Calculations for the Nematic Phase

The orientational ordering of the nematic phase can be described by a traceless and symmetric tensor, defined as: $Q_{ij} = s(n_i n_j - \delta_{ij}/3)$, where s is a scalar order parameter and $\mathbf{n} = (n_1, n_2, n_3)$ is a unit vector representing the director. This Q-tensor formulation is invariant under the transformation $\mathbf{n} \rightarrow -\mathbf{n}$, thereby automatically enforcing inversion symmetry. The free energy, F , of nematic liquid crystals is expressed as (37):

$$F = \int_V dV f_{\text{bulk}} + \int_{\partial V} dS f_{\text{surface}} = \int_V dV (f_{\text{LDG}} + f_{\text{el}}) + \int_{\partial V} dS f_{\text{surface}}. \quad (2)$$

Here the Landau-de-Gennes free energy density f_{LDG} for the nematic phase can be expressed as:

$$f_{\text{LDG}} = \frac{A_0}{2} \left(1 - \frac{U}{3} \right) \text{Tr}(\mathbf{Q}^2) - \frac{A_0 U}{3} \text{Tr}(\mathbf{Q}^3) + \frac{A_0 U}{4} \text{Tr}(\mathbf{Q}^2)^2. \quad (3)$$

The parameter U controls the magnitude of scalar order parameter s at the ground state via $s_0 = \frac{1}{4} + \frac{3}{4} \sqrt{1 - \frac{8}{3U}}$. The Frank-Oseen elastic free energy density, f_{el} , is given as:

$$f_{\text{el}} = \frac{1}{2} L_1 Q_{ij,k} Q_{ij,k} + \frac{1}{2} L_2 Q_{ij,j} Q_{ik,k} + \frac{1}{2} L_3 Q_{kl,i} Q_{kl,j} + \frac{1}{2} L_4 Q_{ik,i} Q_{jl,j}. \quad (4)$$

where L_i are elastic constants, and $Q_{ij,k} \equiv \partial_k Q_{ij}$. The surface anchoring energy can be modelled by the Rapini-Papoular formula: $f_{\text{surface}} = \frac{1}{2} W(\mathbf{Q} - \mathbf{Q}_0)^2$. Here \mathbf{Q}_0 is the surface preferred \mathbf{Q} -tensor, which is determined by the imprinted director patterns at the surfaces.

In numerical calculations, we used $a = \xi_N = 10$ nm as the length unit, where $\xi_N = \sqrt{L_1/A_0}$ is the nematic correlation length, and 10^{-11} N as the force unit. Other parameters used are as follows: $L_1 = 10^{-11}$ N, $L_2 = L_3 = L_4 = 0$ N, $A_0 = 10^5$ J/m³, and $U = 3.5$, leading to $s_0 \cong 0.62$. Unless otherwise specified, we used one-constant-approximation. We set the anchoring on the top and bottom substrates with $W = 10^{-2}$ J/m², and on four side walls with $W = 0$ J/m².

Numerical Calculations for the Ferroelectric Nematic Phase

To calculate the polarization fields in the N_F phase, we adopted a modified Ericksen-Leslie model (38), with the free energy expressed as:

$$F = \int_V (f_{\text{ela}} + f_{\text{grad}} + f_{GL}) dV + \int_S f_{\text{surf}} dS. \quad (5)$$

The elastic energy density f_{ela} is associated with the deformation of the orientation field according to (40):

$$f_{\text{ela}} = \frac{p^2}{2} K_{11} (\nabla \cdot \mathbf{n})^2 + \frac{p^2}{2} K |\nabla \mathbf{n}|^2. \quad (6)$$

The second term represents the energy of any elastic deformations of the orientational field under one equal constant approximation, with K being the elastic constant. In the N_F phase, splay deformations lead to bound charges, as known from the Gauss's law: $\rho = -\nabla \cdot \mathbf{P}$, which increases the free energy because of the depolarization fields (55, 56). This effect can be taken into account by using a relative large splay elastic constant: $K_{\text{splay}} = K_0(1 + \lambda_D^2/\xi_P^2)$, where K_0 is the elastic modulus measured for paraelectric liquid crystals; λ_D is the Debye screening length and ξ_P represents the polarization penetration length. We can assume that $K_{\text{splay}} \gg K$ and add the first term in Eq. (6) to consider the high cost of splay deformations. The real elastic constant for splay deformations becomes: $K_{\text{splay}} = K_{11} + K$.

In this formulation for the free energy, \mathbf{n} is treated as a polar unit vector lacking head-tail symmetry. The polarization is parallel to \mathbf{n} , expressed as $\mathbf{P} \equiv p|P_0|\mathbf{n}$, where the constant P_0 represent the amplitude of the spontaneous polarization, and p is the polar order parameter ranged between 0 and 1. The polar order parameter p is allowed to vary spatially with an energy penalty: $f_{\text{grad}} = \frac{b}{2} |\nabla p|^2$, where b is an elastic constant.

We adopted a Ginzburg-Landau form of the bulk free energy density:

$$f_{GL} = \frac{1}{2} \eta_0 (p - p_0)^2 \quad (7)$$

where η_0 is a material constant. This bulk free energy enforces a preferred polar order p_0 in the bulk. The surface energy is modelled through an expression: $f_{\text{surf}} = \frac{1}{2} W(\mathbf{n} - \mathbf{n}_s)^2$, where \mathbf{n}_s is the surface preferred orientation and W represents the anchoring strength.

The tilt of polarizations at surfaces induces a surface charge density (57): $\sigma_b = \mathbf{P} \cdot \mathbf{v}$, where \mathbf{v} is the surface normal, and causes an increase in the electrostatic energy (58): $U = \frac{1}{8\pi\epsilon_0} \iint \frac{\text{div} \mathbf{P}(\mathbf{r}) \text{div} \mathbf{P}(\mathbf{r}')}{|\mathbf{r} - \mathbf{r}'|} dV' dV$, with ϵ_0 representing the electric constant. We adopted a simplified model in simulations: a strong planar anchoring is used at the top and bottom surfaces to avoid surface charges.

Unless otherwise specified, the following parameters are used: $K_{11} = 20 \text{ pN}$, $K = 1 \text{ pN}$, $p_0 = 0.9$, $b = 1 \text{ pN}$, $\eta_0 = 0.5 \times 10^6 \text{ Jm}^{-3}$ and $W = 0.2 \text{ Jm}^{-2}$.

The free energy in both Eq. (2) and Eq. (5) was minimized using the Euler-Lagrange equation, solved via a finite difference method. This minimization was performed within a cuboid box comprising $101 \times 101 \times 51$ grid points. Periodic boundary conditions were applied for the simulations presented in Fig. 2. For all other simulations, the four side walls were set with zero anchoring strength. We then computed the corresponding optical textures under polarizers from the simulated orientation fields, following a standard procedure detailed in Ref. (59, 60). ParaView, an open-source freeware, was used to visualize the orientation fields.

Acknowledgments

We acknowledge the financial support by National Key Research and Development Program of China under grant 2022YFA1405000, National Nature Science Foundation of China under grants 12174177 and 12204226, Guangzhou Basic and Applied Basic Research Foundation under grant 2024B1515040023, and GJYC Program of Guangzhou via grant 2024D03J0002. We also thank Laurent Bellaiche, Lang Chen, Oleg D. Lavrentovich, Jonathan V. Selinger, Robin B. Selinger and Slobodan Zumer for many valuable discussions.

References

1. N. D. Mermin, The topological theory of defects in ordered media. *Rev. Mod. Phys.* **51**, 591–648 (1979).
2. T. W. B. Kibble, Topology of cosmic domains and strings. *J. Phys. Math. Gen.* **9**, 1387–1398 (1976).
3. A. Vilenkin, E. P. S. Shellard, *Cosmic strings and other topological defects* (2001).
4. V. M. H. Ruutu, *et al.*, Vortex formation in neutron-irradiated superfluid ^3He as an analogue of cosmological defect formation. *Nature* **382**, 334–336 (1996).
5. N. Nagaosa, Y. Tokura, Topological properties and dynamics of magnetic skyrmions. *Nat. Nanotechnol.* **8**, 899–911 (2013).
6. J. Junquera, *et al.*, Topological phases in polar oxide nanostructures. *Rev. Mod. Phys.* **95**, 025001 (2023).
7. M. Kleman, Defects in liquid crystals. *Rep. Prog. Phys.* **52**, 555–654 (1989).
8. I. I. Smalyukh, Review: knots and other new topological effects in liquid crystals and colloids. *Rep. Prog. Phys.* **83**, 106601 (2020).
9. J. V. Selinger, *Introduction to topological defects and solitons: in liquid crystals, magnets, and related materials* (Springer, 2024).
10. W. H. Zurek, Cosmological experiments in superfluid helium? *Nature* **317**, 505–508 (1985).
11. M. B. Hindmarsh, T. W. B. Kibble, Cosmic strings. *Rep. Prog. Phys.* **58**, 477–562 (1995).
12. T. W. B. Kibble, G. Lazarides, Q. Shafi, Walls bounded by strings. *Phys. Rev. D* **26**, 435–439 (1982).
13. J. T. Mäkinen, *et al.*, Half-quantum vortices and walls bounded by strings in the polar-distorted phases of topological superfluid ^3He . *Nat. Commun.* **10**, 237 (2019).
14. I. Chuang, R. Durrer, N. Turok, B. Yurke, Cosmology in the Laboratory: Defect Dynamics in Liquid Crystals. *Science* **251**, 1336–1342 (1991).
15. M. J. Bowick, L. Chandar, E. A. Schiff, A. M. Srivastava, The Cosmological Kibble Mechanism in the Laboratory: String Formation in Liquid Crystals. *Science* **263**, 943–945 (1994).
16. U. Tkalec, M. Ravnik, S. Čopar, S. Žumer, I. Mušević, Reconfigurable Knots and Links in Chiral Nematic Colloids. *Science* **333**, 62–65 (2011).
17. A. Nych, J. Fukuda, U. Ognysta, S. Žumer, I. Mušević, Spontaneous formation and dynamics of half-skyrmions in a chiral liquid-crystal film. *Nat. Phys.* **13**, 1215–1220 (2017).
18. H. Zhao, J.-S. B. Tai, J.-S. Wu, I. I. Smalyukh, Liquid crystal defect structures with Möbius strip topology. *Nat. Phys.* **19**, 451–459 (2023).
19. H. Nishikawa, *et al.*, A Fluid Liquid-Crystal Material with Highly Polar Order. *Adv. Mater.* **29**, 1702354 (2017).
20. R. J. Mandle, S. J. Cowling, J. W. Goodby, A nematic to nematic transformation exhibited by a rod-like liquid crystal. *Phys. Chem. Chem. Phys.* **19**, 11429–11435 (2017).
21. X. Chen, *et al.*, First-principles experimental demonstration of ferroelectricity in a thermotropic nematic liquid crystal: Polar domains and striking electro-optics. *Proc. Natl. Acad. Sci.* **117**, 14021–14031 (2020).
22. O. D. Lavrentovich, Ferroelectric nematic liquid crystal, a century in waiting. *Proc. Natl. Acad. Sci.* **117**, 14629–14631 (2020).
23. E. I. Kats, Combined Defects in Ferroelectric Nematics. *J. Exp. Theor. Phys.* **132**, 641–644 (2021).
24. B. Basnet, *et al.*, Soliton walls paired by polar surface interactions in a ferroelectric nematic liquid crystal. *Nat. Commun.* **13**, 3932 (2022).

25. F. Caimi, *et al.*, Fluid superscreening and polarization following in confined ferroelectric nematics. *Nat. Phys.* **19**, 1658–1666 (2023).
26. J. Yang, Y. Zou, J. Li, M. Huang, S. Aya, Flexoelectricity-driven toroidal polar topology in liquid-matter helielectrics. *Nat. Phys.* **20**, 991–1000 (2024).
27. M. O. Lavrentovich, P. Kumari, O. D. Lavrentovich, Twist, splay, and uniform domains in ferroelectric nematic liquid crystals. *Nat. Commun.* **16**, 6516 (2025).
28. S. Marni, R. Barboza, N. Clark, T. Bellini, L. Lucchetti, Optical Poling of Ferroelectric Liquids. *Adv. Opt. Mater.* **13**, e01378 (2025).
29. Z. Ma, *et al.*, Topological defects induced by air inclusions in ferroelectric nematic liquid crystals with ionic doping. *Soft Matter* **21**, 1333–1340 (2025).
30. Z. Ma, *et al.*, Double Splay Nematic Order in Confined Polar Fluids. *Phys. Rev. Lett.* **134** (2025).
31. Maurice Kleman, Oleg D. Lavrentovich, *Soft Matter Physics* (Springer New York, 2003).
32. Y. Guo, *et al.*, Photopatterned Designer Disclination Networks in Nematic Liquid Crystals. *Adv. Opt. Mater.* **9**, 2100181 (2021).
33. H. Yun, *et al.*, Ultra-high spatial resolutions in photopatterning molecular orientations. *Opt. Express* **32**, 31107 (2024).
34. P. Kumari, B. Basnet, M. O. Lavrentovich, O. D. Lavrentovich, Chiral ground states of ferroelectric liquid crystals. *Science* **383**, 1364–1368 (2024).
35. L. Paik, J. V. Selinger, Flexoelectricity versus electrostatics in polar nematic liquid crystals. *Phys. Rev. E* **111**, L053402 (2025).
36. T. Emersic, J. J. De Pablo, A. Snezhko, A. Sokolov, Dynamics of Acoustically Energized Active Nematic Droplets. *Phys. Rev. Lett.* **135**, 048301 (2025).
37. M. Ravnik, S. Žumer, Landau–de Gennes modelling of nematic liquid crystal colloids. *Liq. Cryst.* **36**, 1201–1214 (2009).
38. Y. Han, J. Yin, Y. Hu, A. Majumdar, L. Zhang, Solution landscapes of the simplified Ericksen–Leslie model and its comparison with the reduced Landau–de Gennes model. *Proc. R. Soc. Math. Phys. Eng. Sci.* **477**, 20210458 (2021).
39. S. Yi, *et al.*, Chiral π domain walls composed of twin half-integer surface disclinations in ferroelectric nematic liquid crystals. *Proc. Natl. Acad. Sci.* **121**, e2413879121 (2024).
40. P. Kumari, *et al.*, Conic sections in ferroelectric nematics: Experiments and mathematical modeling. *Phys. Rev. Res.* **6**, 043207 (2024).
41. N. Sebastián, *et al.*, Ferroelectric-Ferroelastic Phase Transition in a Nematic Liquid Crystal. *Phys. Rev. Lett.* **124**, 037801 (2020).
42. N. Sebastián, *et al.*, Polarization patterning in ferroelectric nematic liquids via flexoelectric coupling. *Nat. Commun.* **14**, 3029 (2023).
43. S. Marni, *et al.*, Fluid jets and polar domains, on the relationship between electromechanical instability and topology in ferroelectric nematic liquid crystal droplets. *Soft Matter* **20**, 4878–4885 (2024).
44. J.-T. Pan, *et al.*, Nonlinear geometric phase coded ferroelectric nematic fluids for nonlinear soft-matter photonics. *Nat. Commun.* **15**, 8732 (2024).
45. K. M. Rabe, C. H. Ahn, J.-M. Triscone, Eds., *Physics of ferroelectrics: a modern perspective* (Springer, 2007).
46. A. K. Yadav, *et al.*, Observation of polar vortices in oxide superlattices. *Nature* **530**, 198–201 (2016).
47. S. Das, *et al.*, Observation of room-temperature polar skyrmions. *Nature* **568**, 368–372 (2019).

48. Y. J. Wang, *et al.*, Polar meron lattice in strained oxide ferroelectrics. *Nat. Mater.* **19**, 881–886 (2020).

49. J. Karcz, *et al.*, Spontaneous chiral symmetry breaking in polar fluid–heliconical ferroelectric nematic phase. *Science* **384**, 1096–1099 (2024).

50. C. J. Gibb, *et al.*, Spontaneous symmetry breaking in polar fluids. *Nat. Commun.* **15**, 5845 (2024).

51. H. Nishikawa, *et al.*, Emergent Ferroelectric Nematic and Heliconical Ferroelectric Nematic States in an Achiral “Straight” Polar Rod Mesogen. *Adv. Sci.* **11**, 2405718 (2024).

52. J. Li, *et al.*, Development of ferroelectric nematic fluids with giant- ϵ dielectricity and nonlinear optical properties. *Sci. Adv.* **7**, eabf5047 (2021).

53. V. Sultanov, *et al.*, Tunable entangled photon-pair generation in a liquid crystal. *Nature* **631**, 294–299 (2024).

54. C.-Y. Li, *et al.*, Domain engineering in ferroelectric nematics for nonlinear optical modulation. *Sci. Adv.* **11**, eadu7362 (2025).

55. K. Okano, Electroslatice Contribution to the Distortion Free Energy Density of Ferroelectric Liquid Crystals. *Jpn. J. Appl. Phys.* **25**, L846 (1986).

56. J.-B. Lee, R. A. Pelcovits, R. B. Meyer, Role of electrostatics in the texture of islands in free-standing ferroelectric liquid crystal films. *Phys. Rev. E* **75**, 051701 (2007).

57. P. Kumari, B. Basnet, H. Wang, O. D. Lavrentovich, Ferroelectric nematic liquids with conics. *Nat. Commun.* **14**, 748 (2023).

58. R. B. Meyer, L. Liebert, L. Strzelecki, P. Keller, Ferroelectric liquid crystals. *J. Phys. Lett.* **36**, 69–71 (1975).

59. G. Poy, S. Žumer, Ray-based optical visualisation of complex birefringent structures including energy transport. *Soft Matter* **15**, 3659–3670 (2019).

60. G. Poy, S. Žumer, Physics-based multistep beam propagation in inhomogeneous birefringent media. *Opt. Express* **28**, 24327 (2020).

Figures

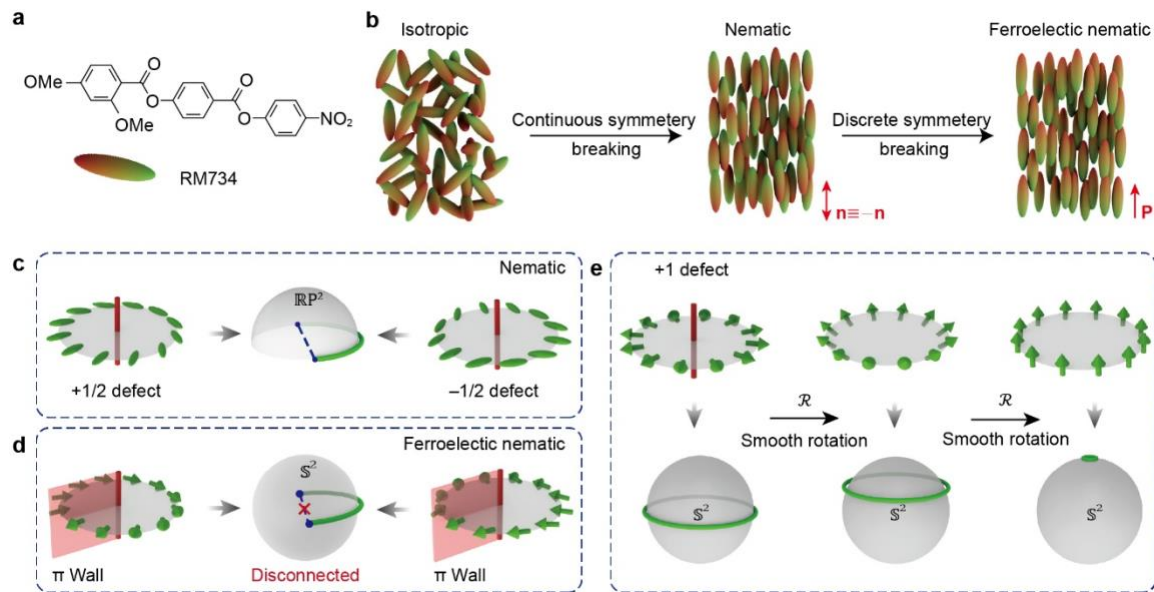


Figure 1. Phase transition, ground state manifold and topological defect. (a, b) Chemical structure (a) and phase transitions (b) of the ferroelectric liquid crystal material RM734. (c, d) Mapping of director and polarization on a loop encircling $\pm 1/2$ defects to the ground state manifold in the N (c) and the N_F (d) phase. (e) Continuous transformation of a +1 line defect into a uniform (topologically trivial) state, illustrating topological instability of integer disclinations in the N_F phase.

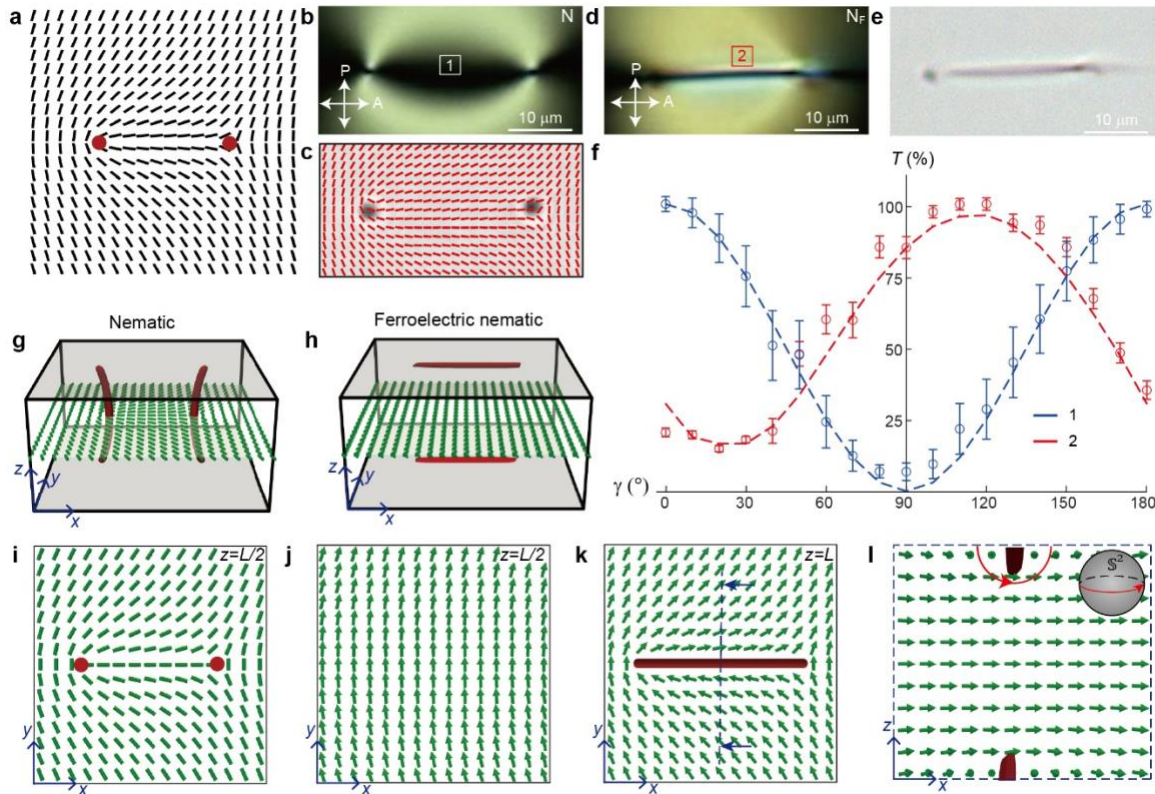


Figure 2. Transformation of $\pm 1/2$ disclination into domain wall. (a) Director field of the $\pm 1/2$ defect pair. (b, c) Polarizing optical image (b) and corresponding measured director field (c) in the N phase; the background in (c) is a bright-field image. (d, e) Polarizing optical (d) and bright-field (e) images of the domain wall in the NF phase. The cell thickness is $L=1.5$ μm . (f) Optical transmittance measured in regions 1 (b) and 2 (d) as a function of the analyzer–polarizer angle γ ; dashed curves show calculated transmittance from the simulated orientation field. (g, h) Numerically calculated defect configurations in the N (g) and NF (h) phases. (i, j) Calculated director and polarization fields at the cell midplane in the N (i) and NF (j) phases. (k) Calculated polarization field in the xy plane near the top confining substrates. (l) Calculated polarization field in the cross-sectional plane indicated by the dashed line in (k). The mapping of the surface defect traces out a half-circle on the ground state manifold, indicating a half-integer strength. Dark brown regions in (g, h, k, l) denote areas where the order parameters s and p fall below 0.45.

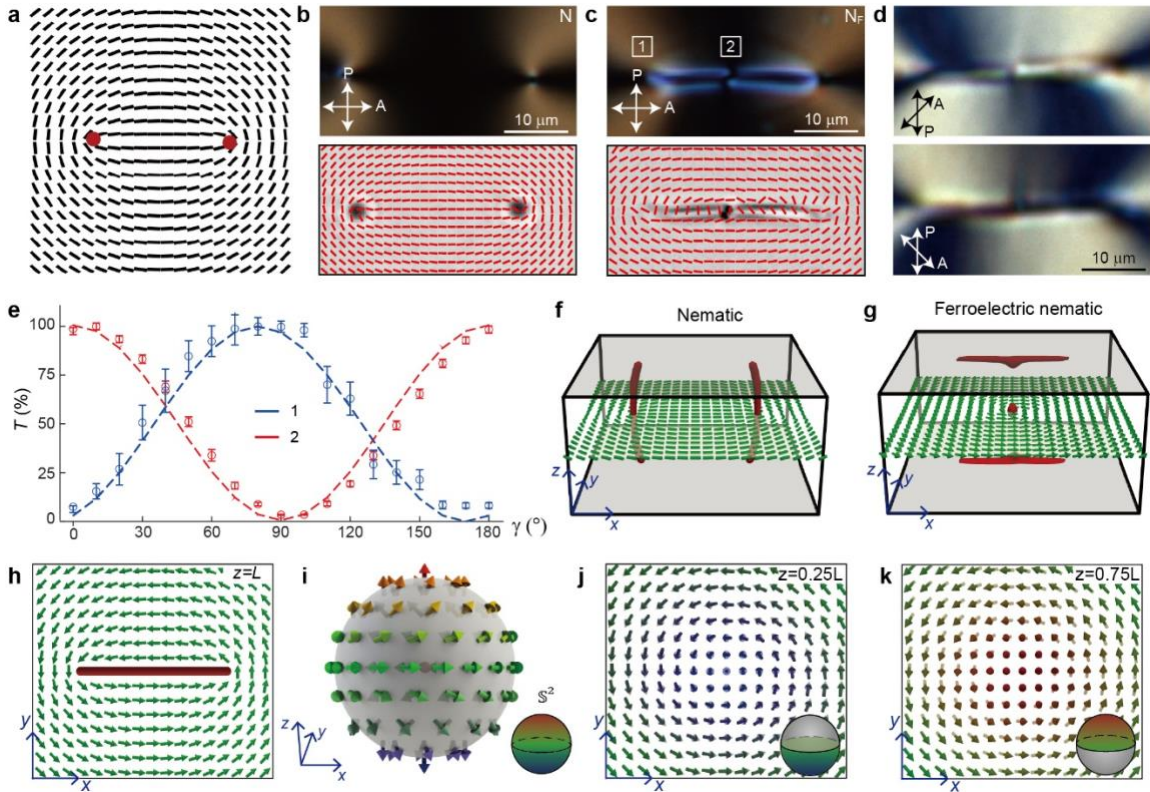


Figure 3. Transformation of a $+1/2$ disclination pair into a monopole-embedded domain wall.
 (a) Director field of the $+1/2$ defect pair. (b, c) Polarizing optical images (top) and measured director fields (bottom) in the N phase (b) and N_F phase (c). (d) Polarizing optical images of the N_F defect with the analyzer oriented at 45° and 135° relative to the polarizer. Cell thickness: $L = 2.0 \mu\text{m}$. (e) Optical transmittance in regions 1 and 2 of (c) as a function of analyzer–polarizer angle γ ; dashed curves show calculated transmittance from the simulated director field. (f, g) Simulated defect configurations in the N (f) and N_F (g) phases. (h-k) Calculated polarization fields near the top substrate (h), on a spherical surface encompassing the monopole and its mapping into the ground-state manifold (i), and within xy -planes at $z = 0.25L$ (j) and $z = 0.75L$ (k). Dark brown regions in (f, g, h) denote areas where the order parameters s and p fall below 0.45. The color of the arrows (\mathbf{P}) and of the ground state manifold \mathbb{S}^2 in (i-k) represents the polar angle between \mathbf{P} and z-axis.

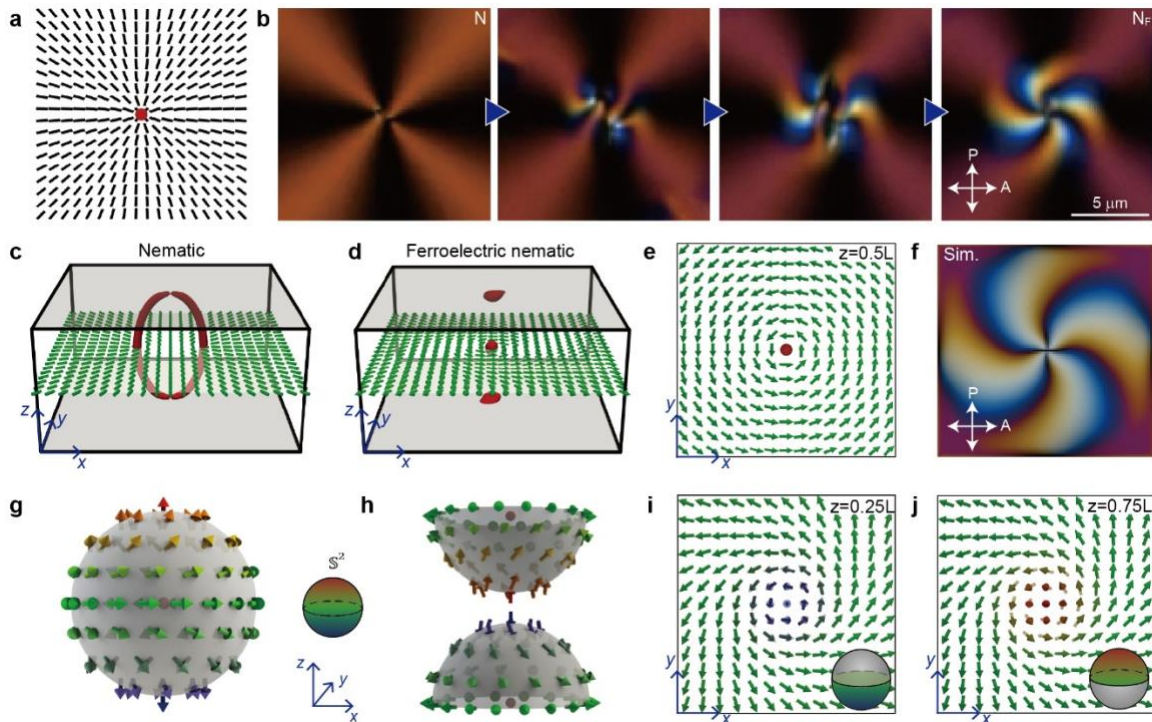


Figure 4. Transformation of a radial +1 disclination into a meron-mediated monopole and boojums. (a) Director field of the radial +1 defect. (b) Polarizing optical images of the evolving +1 defect upon quenching from the N to the N_F phase. Cell thickness: $L = 2.6 \mu\text{m}$. (c, d) Simulated defect structures in the N (c) and the N_F (d) phases. (e) Simulated polarization field at the cell midplane. (f) Calculated polarized optical texture using the simulated director field. (g) Calculated polarization field on a spherical surface encompassing the monopole. (h) Calculated polarization fields on hemispherical surfaces encompassing the boojums at the top and bottom substrates. (i, j) Calculated polarization fields in xy-planes at $z = 0.25L$ (i) and $z = 0.75L$ (j). Dark brown regions in (c, d) denote areas where the order parameters s and p fall below 0.45. The color of the arrows and of the ground state manifold \mathbb{S}^2 in (g-j) represents the polar angle between \mathbf{P} and z-axis.